

Reversing Hydrogen-Related Loss in α -Ta Thin Films for Quantum Device Fabrication

D. P. Lozano¹, M. Mongillo¹, B. Raes¹, Y. Canvel¹, S. Massar¹, A. M. Vadiraj¹, Ts. Ivanov¹, R. Acharya¹, J. Van Damme^{1,2}, J. Van de Vondel³, D. Wan¹, A. Potočník¹, and K. De Greve^{1,2}

¹Imec, Kapeldreef 75, Leuven, B-3001, Belgium,

²Department of Electrical Engineering (ESAT), KU Leuven, Leuven, B-3000, Belgium

³Department of Physics and Astronomy, KU Leuven, Leuven, B-3000, Belgium

Email: daniel.perezlozano@imec.be

Email: anton.potocnik@imec.be

Abstract

α -Tantalum (α -Ta) is an emerging material for superconducting qubit fabrication due to the low microwave loss of its stable native oxide. However, hydrogen absorption during fabrication, particularly when removing the native oxide, can degrade performance by increasing microwave loss. In this work, we demonstrate that hydrogen can enter α -Ta thin films when exposed to 10 vol% hydrofluoric acid for 3 minutes or longer, leading to an increase in power-independent ohmic loss in high-Q resonators at millikelvin temperatures. Reduced resonator performance is likely caused by the formation of non-superconducting tantalum hydride (TaH_x) precipitates. We further show that annealing at 500°C in ultra-high vacuum (10^{-8} Torr) for one hour fully removes hydrogen and restores the resonators' intrinsic quality factors to ~ 4 million at the single-photon level. These findings identify a previously unreported loss mechanism in α -Ta and offer a pathway to reverse hydrogen-induced degradation in quantum devices based on Ta and, by extension also Nb, enabling more robust fabrication processes for superconducting qubits.

Keywords: superconductors, alpha-Ta, high-Q resonators, quantum computing, tantalum hydride, ohmic loss

Introduction

Superconducting qubits have garnered significant attention in quantum information technologies due to their scalability and high-gate fidelity.¹ Despite considerable advancements in qubit performance over the past two decades, further improvements in coherence times and fidelity are essential for realizing practical, large-scale quantum computers based on superconducting qubits.² Among the various sources of decoherence, fabrication processes play a critical role, as they can introduce defects and impurities that contribute to microwave loss that in turn limit coherence: examples of such defects include two-level systems and excess quasiparticles.³⁻⁵ To achieve high coherence while maintaining compatibility with industrial-scale methods, qubit fabrication can leverage processing techniques borrowed from the complementary metal-oxide-semiconductor (CMOS) industry.⁶

α -Tantalum (α -Ta) has recently emerged as a promising material for superconducting qubits due to its favorable morphological and superconducting properties, including low microwave loss of its stable native oxide.⁷⁻¹³ These characteristics make α -Ta a strong alternative to aluminium (Al) and niobium (Nb),¹⁴ which are widely used in superconducting qubit fabrication.⁴ In particular, Ta's native oxide exhibits a more stable and well-coordinated atomic structure with lower oxygen deficiency compared to Nb oxides, likely resulting in lower magnetic moments density.¹⁵ Despite these advantages, α -Ta—like Nb—has a high hydrogen solubility due to its large interstitial sites in the body-centered-cubic (bcc) crystal structure.¹⁶⁻¹⁸

The presence of diluted hydrogen in Nb metal has been linked to a reduction of high Q-factors in superconducting radio frequency cavities¹⁹⁻²¹ and, more recently, in planar superconducting Nb resonators²² fabricated using processes similar to those of superconducting qubits.^{23,24} Hydrogen absorption in Nb—and likely also in α -Ta films—can occur during various fabrication steps, particularly when the protective native oxide layer, which serves as a hydrogen diffusion barrier,^{21,22,25} is removed. Hydrogen incorporation can take place during oxide cleaning with fluorine-based etchants, such as hydrofluoric acid (HF)^{9,26} or buffered oxide etchant (BOE),^{10,11,27} both commonly used to remove surface oxides and passivate silicon-air interface. Additionally, hydrogen can enter the metal during acidic or hydrogen-rich etching processes (e.g. chlorine- or fluorine-based wet⁷ or dry^{8,9,14} etching), either through the exposed metal surface during etching or at the sidewalls after etching, where the metal remains unprotected. Furthermore, exposure of unoxidized Nb or Ta films to ambient conditions can also lead to hydrogen absorption from the atmosphere.

While the presence of hydrogen, in the form of NbH_x precipitates,^{21,23} and its detrimental impact on microwave loss in high-Q resonators²² have been established for Nb-based devices, no evidence of TaH_x formation or its potential effect on high-Q resonators and qubits has been reported or systematically investigated for α -Ta thin films.

In this study, we investigate the impact of hydrogen absorption in α -Ta thin films, with a particular focus on its effect on microwave loss relevant to superconducting qubit performance. We show that hydrogen can diffuse into α -Ta in an acidic environment, increasing power-independent ohmic loss and suppressing resonance features in superconducting resonators at millikelvin temperatures, likely due to the formation of non-superconducting tantalum hydride (TaH_x) precipitates. However, we also demonstrate that annealing these films in ultra-high vacuum (UHV) at 500°C for one hour removes hydrogen and fully restores the resonators' quality factors. These findings enable the use of a broader range of etchants for faster and more aggressive surface cleaning and oxide removal, while

also providing a technique to reverse the detrimental effects of hydrogen absorption in Ta-based quantum devices.

Methodology

Hydrogen incorporation into α -Ta films is achieved through a hydrofluoric acid (HF) surface oxide removal process.²⁶ Samples with patterned coplanar waveguide resonators on α -Ta films and silicon wafers, fabricated using the high-temperature process described in Ref. 9, are submerged in 10 vol% diluted HF for varying durations: 0 min (reference), 1 min, 2 min, 3 min, 5 min, and 10 min. Immediately after the HF treatment, the samples are rinsed in deionized water until the water resistivity in the bath exceeded 12 M Ω .

Hydrogen absorption into the α -Ta films and further modifications due to the HF treatment are investigated thoroughly on patterned samples with the following material characterization techniques: scanning transmission electron microscopy (STEM), time-of-flight secondary ion mass spectrometry (ToF-SIMS), elastic recoil detection analysis (ERDA), atomic force microscopy (AFM) and X-ray photoelectron spectroscopy (XPS). The same set of samples is used for ToF-SIMS, AFM and XPS measurements and different sets are used for the STEM and ERDA measurements (see Methods section). In addition to the morphological investigations, high-Q resonator measurements are performed at 10 mK in a standard dilution refrigerator designed for high-coherence superconducting qubit measurements (see Methods section).⁹

Results and discussion

Morphology

STEM analysis reveals that the etching process initiates at the triple point—where the metal-air, substrate-air, and substrate-metal interfaces intersect (Figure 1a). At this location, a small gap forms once SiO_x is removed by HF (after ~1 min²⁶), exposing the Ta film and making it susceptible to etching. As the duration of HF exposure increases, the etched area gradually extends deeper into the film. The same behaviour is observed on several samples, four of which are presented in Figure 1a. STEM micrographs suggest that the triple point serves as the primary pathway for hydrogen infiltration into the film. This is supported by the observation that other regions, specifically the top Ta surface and a large part of the sidewall remain resistant to etching for at least the first ~5 minutes of HF exposure. After this time, the HF starts inducing substantial surface modification, indicated by the AFM measurements in (Figure 1b,c). After 10 minutes HF removes approximately ~50 nm of tantalum from the sidewall and ~40 nm from the top surface. The observed difference in etching behavior arises from the varying chemical reactivity of pure α -Ta and tantalum oxide. Experiments demonstrate that even a brief 1-minute exposure to the HF solution is sufficient to initiate etching of unprotected α -Ta with an etching rate of approximately 15 nm/min. In contrast, tantalum oxide exhibits significantly greater resistance, with an estimated etching rate of ~0.4 nm/min—a value that aligns with previously reported findings in the literature²⁸ (see Supplemental Information).

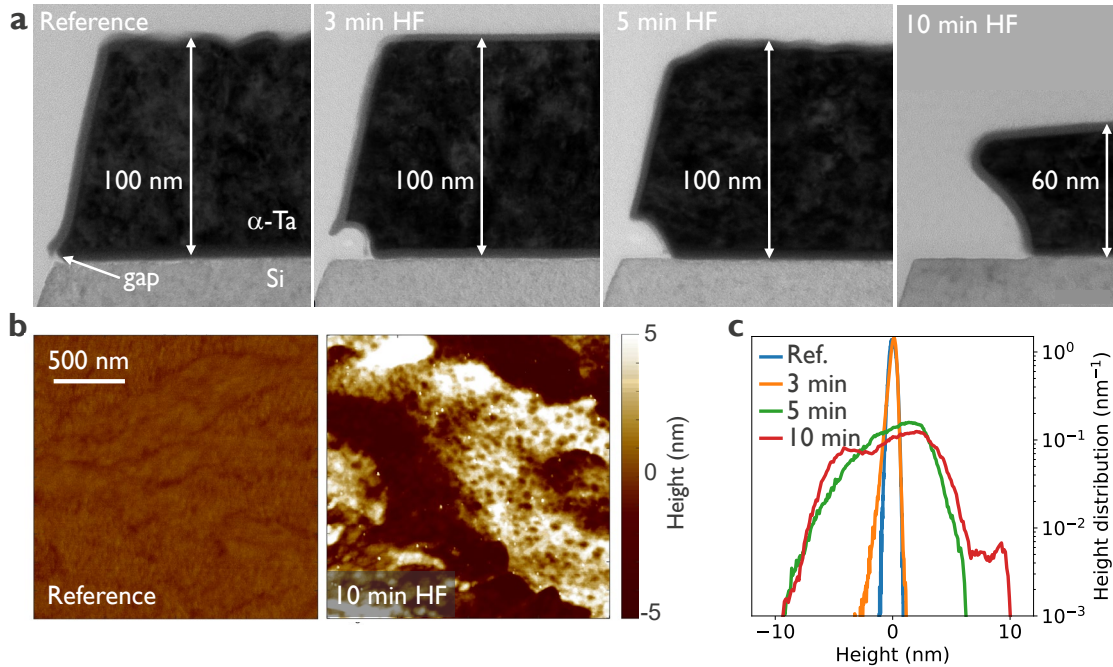


Figure 1: Ta resonators exposed to diluted HF for different durations. **a** cross-STEM micrographs. **b** AFM topography of the Ta top surface for selected reference and 10-minute HF sample. AFM images of all other samples are shown in the Supplementary Information. **c** Height probability density measured with AFM across the $2 \mu\text{m} \times 2 \mu\text{m}$ area. Root-mean-square roughness (R_q) values for reference, 3 min, 5 min and 10 min samples are 0.28 nm, 0.38 nm, 2.65 nm and 3.30 nm, respectively.

Hydrogen content

The presence of hydrogen diluted in Ta films is first investigated with a ToF-SIMS measurements. To avoid hydrogen atoms rapidly discharging from the film into the high vacuum of the sample chamber as soon as the native oxide is sputtered away²⁵ an oxygen (O_2) sputtering beam is employed, which oxidizes the surface and prevents premature hydrogen desorption during the ToF-SIMS measurement. The background level of hydrogen is $\sim 4 \cdot 10^{-4}$ in the untreated reference Ta sample (Figure 2a). Similar levels are found in samples exposed to HF for 2 min (Supplementary Information). The amount of detected hydrogen starts increasing at 3 min and reaches levels of $\sim 1 \cdot 10^{-2}$ at 10 min exposure duration (Figure 2b,c,d). The detection of elevated hydrogen (H^+) levels throughout the film in the 3-minute sample, combined with the presence of an oxide layer on all other surfaces acting as a strong hydrogen diffusion barrier, suggests that a significant amount of hydrogen is absorbed through the triple points and relatively quickly spread throughout the thin film. This is supported by the fact that the diffusion coefficient of hydrogen in Ta is approximately $10^{-6} \text{ cm}^2/\text{s}$ at room temperature,^{17,18} allowing hydrogen to diffuse across hundreds of micrometres within minutes. In contrast to H^+ , tantalum hydride species (Ta_2H^+ , TaH_5^+ , and TaH_x^+) are either absent or show levels comparable to the background.

To further confirm the presence of hydrogen in the HF treated α -Ta samples and identify possible tantalum hydride phases²⁹, elastic recoil detection analysis (ERDA) is performed next to quantitatively determine the atomic fraction of hydrogen in the metal. For the reference, 2 min, and 3 min samples, the hydrogen atomic fraction is comparable, ranging from 3% to 4% (Figure 2e), qualitatively consistent with the ToF-SIMS data. At these levels, hydrogen is randomly filling predominantly tetragonal interstitial sites in the bcc α -Ta at room temperature, resulting in a disordered solution of hydrogen in tantalum. In the 5 min sample, however, the hydrogen atomic fraction increases to $\sim 12\%$, placing it at the boundary between the α -Ta and α -Ta + ϵ phases,^{29,30} suggesting that ϵ -tantalum hydride (ϵ - Ta_2H) may also be

present. For the 10 min HF sample, the hydrogen atomic fraction reached 40%-45%, making δ -tantalum hydride (δ -Ta₂H) a plausible phase in the film.

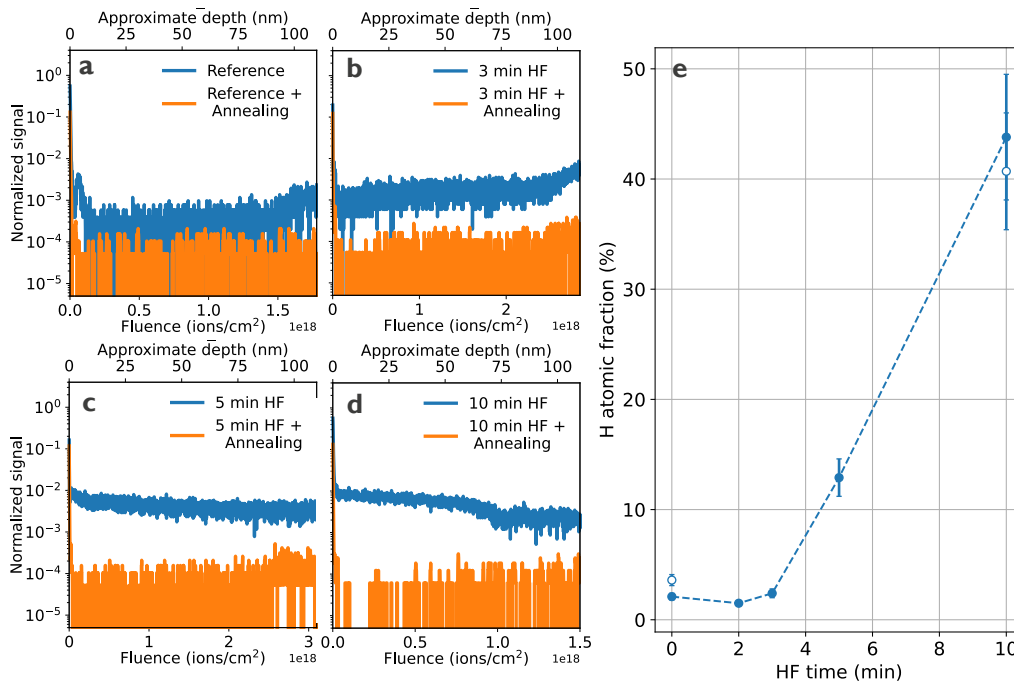


Figure 2: ToF-SIMS hydrogen signal (normalized counts per second) as a function of fluence or approximate depth for **a** reference, **b** 3 min, **c** 5 min and **d** 10 min HF exposure. Results from samples subjected to a subsequent annealing are plotted in orange color. Silicon signal (not shown here) starts at an approximate depth of 100 nm. **e** Energy Recoil Detection Analysis (ERDA) results showing hydrogen atomic fraction as a function of HF exposure time. Empty symbols present additional measurements on a separate set of reference and 10 min HF samples to test reproducibility. Dashed line is a guide to the eye. Measurements are performed on the Ta surface hundreds of micrometers away from patterned edges.

Superconducting transition temperature measurements show that Ta films exposed to HF for 10 minutes do not exhibit superconductivity, whereas films subjected to shorter exposures remain superconducting (see Figure S7 in Supplementary Information). Furthermore, given that the only known superconducting tantalum hydride forms under extreme pressure (197 GPa),³¹ we hypothesize that any TaH_x precipitates remain metallic at cryogenic temperatures and lead to ohmic loss. These findings suggest that excessive hydrogen incorporation can severely degrade superconducting properties, potentially leading to increased energy loss in superconducting qubits and reduced coherence times.

To eliminate the detrimental effects of hydrogen incorporation, an annealing procedure is employed to fully desorb hydrogen from the α -Ta film.²⁹ This approach is similar to previously demonstrated methods for hydrogen removal in bulk Nb films.³² The annealing process of HF-treated samples is carried out at 500°C for one hour under high vacuum ($\sim 10^{-8}$ Torr). The removal of hydrogen from the film is confirmed by ToF-SIMS, where the H⁺ signal in all annealed samples after HF treatment returns to background levels (orange datapoints in Figure 2a,b,c,d). While prolonged HF exposure strongly affects the metal surface roughness, high-vacuum annealing does not further modify the surface (see Supplementary Information).

Chemical analysis

A more comprehensive understanding of the chemical changes and surface oxidation in tantalum films, resulting from HF treatment and subsequent high-vacuum annealing, is obtained through XPS analysis on the Ta top surface, hundreds of micrometers away from the patterned structures. Binding energy spectra show two Ta4f doublets (Figure 3a). The

first at 28.0 eV and 26.2 eV, corresponds to Ta4f_{5/2} and Ta4f_{7/2} peaks of Ta₂O₅ and the second doublet at 22.6 eV and 20.7 eV corresponds to the metallic Ta4f_{5/2} and Ta4f_{7/2} peaks, respectively. The ratio of the Ta₂O₅/Ta peak amplitudes decreases with HF exposure duration, indicating that the HF treatment removes excess Ta oxide from the surface (see supplementary information and Figure S6 for more details).

Interestingly, a significant shift of the metallic Ta doublet is observed with increasing HF duration. In the 10-minute HF sample, the Ta4f_{5/2} and Ta4f_{7/2} peaks shift from 22.6 eV to 23.3 eV and from 20.7 eV to 21.4 eV, respectively, compared to the reference sample. This is clearly visible in the binding energy shift, calculated as a binding energy difference between the Ta₂O₅ and the metallic Ta4f_{7/2} peaks (Figure 3c). To confirm that this shift is not a measurement artifact, the measurements are repeated on two additional sets of samples, which consistently show the same trend (see Supplementary Information). The observed binding energy shift is not related to charging effects, as this would result in the opposite effect, where instead of metallic, the oxide peak would gradually shift to higher energies, and the metallic peak would remain unaffected.³³

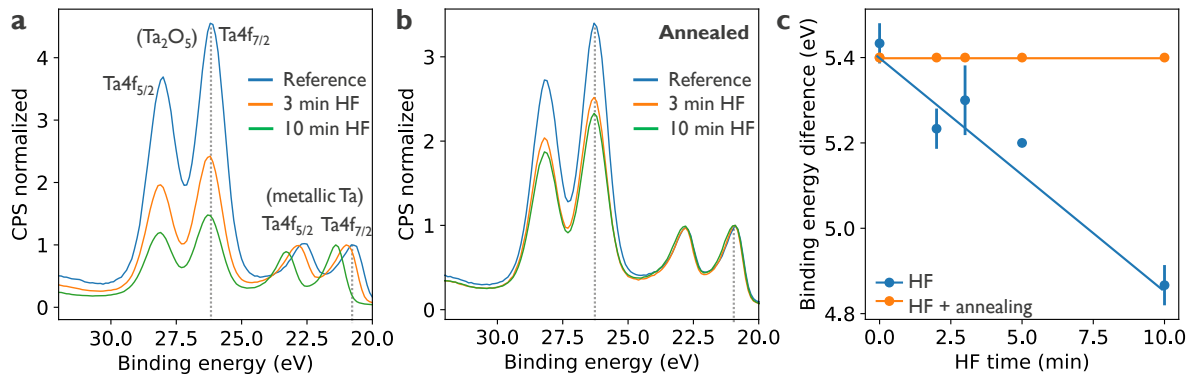


Figure 3: **a** Ta binding energy spectrum (normalized counts per second) obtained with surface XPS for selected reference, 3 min HF and 10 min HF samples. **b** similar to **a** but, with an additional annealing step. Spectra are normalized to the intensity of the metallic Ta4f_{7/2} peak. **c** binding energy difference for the HF treated samples with and without the high vacuum annealing. The difference is calculated based on Ta4f_{7/2} peak indicated with dashed vertical lines.

The observed binding energy shift is postulated to result from hydride formation in the film. Absorbed hydrogen could alter the electronic environment of tantalum, leading to a shift of the Ta4f electrons to higher binding energies. Moreover, the fact that only the metallic peaks are affected and not the oxide peaks indicates that hydrogen is only absorbed in the tantalum metal and not in the oxide. This is further supported by the XPS results from annealed samples, where no shift in the metallic Ta doublet (Figure 3b) and the associated binding energy difference (orange points in Figure 3c) is observed with increasing HF exposure time. This indicates that hydrogen desorption restores the electronic environment of the Ta lattice to that of the reference untreated sample. To our knowledge this is the first time such binding energy shift is reported, since no reference for tantalum hydrides are present in well-known XPS databases.³⁴

Microwave loss

The impact of hydrogen incorporation in α -Ta film on microwave loss is evaluated by measuring the intrinsic quality factor (Q_i) of high-Q resonators in a dilution refrigerator at ~ 10 mK temperature (see Methods for details). Resonators serve as effective proxies for superconducting qubits, as they are sensitive to many of the same microwave loss mechanisms while being easier and faster to fabricate and measure. Each sample contains eight coplanar-waveguide resonators with resonant frequencies evenly distributed between 4.2 and 7.8 GHz.

All resonators share the same geometry, with a central trace width of $w = 24 \mu\text{m}$ and a gap of $s = 12 \mu\text{m}$ between the trace and the ground plane.

The resonator internal Q -factor characterization is performed on all resonators across differently processed samples to obtain statistically relevant results. For clarity, only single-photon level (low-power) $Q_{i,LP}$ and high-power $Q_{i,HP}$ datapoints in the linear regime (up to $\sim 10^8$ photons) are shown in Figure 4a. A pair of $Q_{i,LP}$ - $Q_{i,HP}$ datapoints is connected by a vertical line for each resonator. Resonators exposed to HF for 1 min and 2 min exhibit approximately twice the median $Q_{i,LP}$ ($\sim 4\text{M}$) compared to the reference sample ($Q_{i,LP}$, $\sim 2\text{M}$), consistent with our previous findings.⁹ Resonators exposed to HF for 3 min show a notable decrease in Q_i factors down to $Q_{i,LP} \sim 1\text{M}$, and a negligible power dependence. This indicates that already low amounts of absorbed hydrogen in the 3-min HF sample ($\sim 4\%$ atomic fraction, see Figure 2e) is sufficient to degrade the resonator performance. In samples exposed to HF for 5 min and 10 min, resonances could still be detected, but with drastically lower Q_i values of $\sim 10^4$ and ~ 200 , respectively. These resonances are particularly challenging to detect and analyze due to the large mismatch between internal and coupling quality factors. Notably, annealing restores internal Q -factors for all HF-treated samples, including the 5- and 10-minute samples (orange points in Figure 4a), confirming that the observed microwave loss mechanism is linked to the presence of hydrogen in α -Ta films.

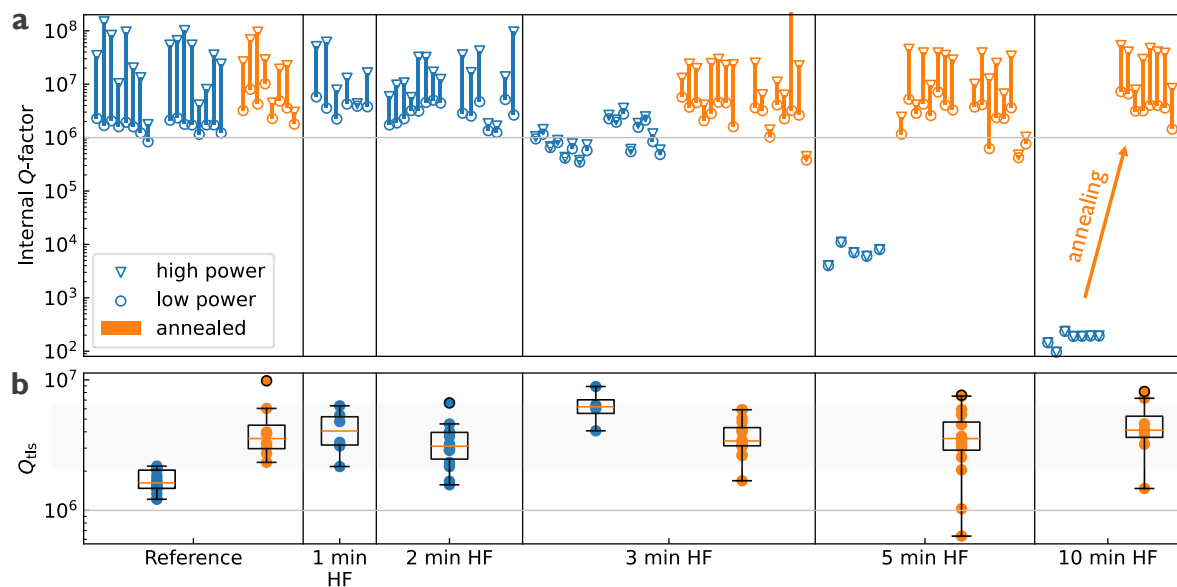


Figure 4: High- Q resonator measurement results. **a** high power (triangle) and low power (circle) internal Q -factor datapoints are connected with a vertical line for each resonator. Datapoints corresponding to resonators from different samples are separated with a larger gap in horizontal direction than datapoints corresponding to the same sample. Resonators are horizontally ordered according to their frequency. Samples subject to UHV annealing are plotted with the orange color. While time dependence of low power Q_i was measured for selected resonators (not shown), their standard deviation is generally lower than resonator-to-resonator variation. **b** Extracted Q_{TLS} for all measured resonators are grouped together on a strip plot grouped by different sample treatments. Box plot is added to each strip plot, where the box extends from the lower to upper quartile values of the data, with a line at the median. The whiskers extend from the box and show the range of the data up to 1.5x the inter quartile range (IQR). Flier datapoints beyond that range are considered outliers.

To distinguish power-dependent TLS loss from the power-independent loss, all extracted Q_i in the linear regime (powers below nonlinear Duffing behavior) as a function of photon number are fitted using a TLS model [Eq. (2) in Methods] for different samples (Figure 4b). This analysis reveals that TLS loss ($1/Q_{TLS}$) is not affected by HF exposure up to 3 minute, while the power-independent loss increases with longer HF exposure affecting both high-power and low-power Q_i (Figure 4a). Furthermore, after annealing the 3-, 5- and 10-minute

samples exhibit a restored power dependence of Q_i , with TLS loss comparable to that of unannealed 1- and 2-minute HF samples with $Q_{\text{TLS}} \sim 4\text{M}$. For the summary of all fitting parameters see Figure S9.

It is worth noting that after annealing, the 5- and 10-minute HF-treated samples show approximately ten times higher Ta surface roughness compared to the reference sample (Figure 1b,c and Figure S3). This increased roughness is expected to enhance the participation ratio of the metal-air interface.⁴ However, Q_{TLS} in these samples remains comparable to that of samples with shorter HF exposure and lower surface roughness. Since the annealing and deposition temperatures are comparable (500°C), the silicon-metal interface is not expected to be affected by annealing. The consistent Q_{TLS} across all HF-treated samples suggests that the dominant loss mechanism does not originate from the metal-air interface (tantalum oxide).

It is also interesting to note that Q_{TLS} of the annealed reference sample is approximately two times higher than that of the non-annealed reference samples. Since the reference samples contain SiO_x , the increased Q_{TLS} after annealing could be attributed to SiO_x modification or TaO_x reduction (Figure S6). However, further investigation is needed to determine the exact mechanism behind the TLS loss reduction during annealing.

Further insight into the role of hydrogen in superconducting circuits is gained by analyzing the performance of resonators at high powers levels, beyond the linear regime. At microwave powers above $\sim 10^8$ photons, superconducting high-Q resonators typically exhibit Kerr-type nonlinear behaviour.³⁵⁻³⁹ Interestingly, the 3-minute HF sample displays this nonlinear response at much lower photon numbers, around $\sim 10^3$. In addition to the Kerr-type nonlinear frequency shift, an increase in microwave loss can be observed as the photon number increases (empty blue circles in Figure 5a). This power dependence is well described by a two-photon loss mechanism, which is associated with quasiparticle heating.^{35,36} Further supporting this interpretation, the measured scattering parameter S_{21} data in the IQ plane exhibit an elliptical shape (Figure 5c), a characteristic signature of two-photon loss.³⁵ Fitting a nonlinear model to the measured scattering parameters allows to extract Kerr (K_{nl}) and two-photon (γ_{nl}) parameters, which are consistent across all resonators on this sample and range between 0.5 kHz and 3 kHz (Figure S8). For further details on the nonlinear model, see the Nonlinear resonator modeling section in the Supplementary Information).

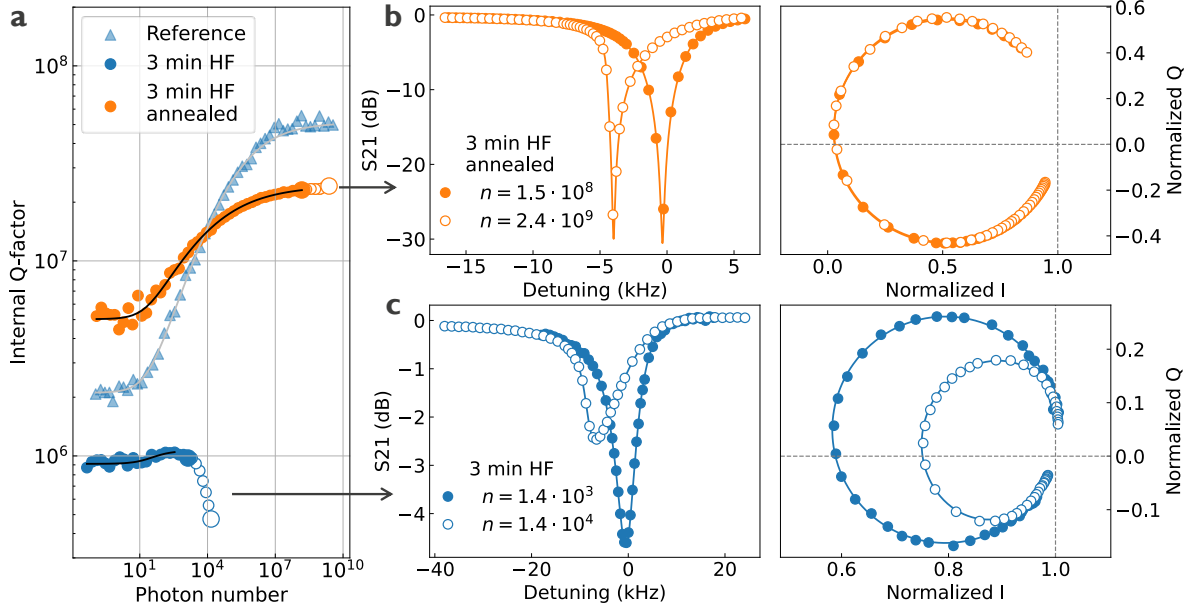


Figure 5: Power dependent internal Q -factor measurement. **a** Power or photon number dependent internal Q -factor for resonator R1 on samples exposed to different treatments indicated in the legend. Filled markers are obtained by fitting the scattering parameter data to a linear model (Eq. 1 in Methods) and empty markers are obtained by using a nonlinear model (Eq. 8 in Supplementary Information). **b** Scattering parameters as a function of frequency for sample placed in HF for 3 min and received subsequent annealing treatment. The two traces correspond to a linear and nonlinear regime indicated with a photon number in the legend and with large markers in panel **a**. **c** The same as for panel **b**, but on 3 min HF sample that was not thermally treated. In the later one, non-circular IQ trace is clearly visible indicating the presence of nonlinear two-photon energy loss in high- Q resonators.

After annealing the 3-min HF sample, the high-power behavior of the Q_i recovers, exhibiting the expected Kerr-type nonlinearity at expected high photon numbers ($\sim 10^8$ and above). The S_{21} data in the IQ plane retains a fully circular trace, and the extracted Kerr parameter decreases significantly to $K_{nl} = 5 \times 10^{-6}$ Hz at $n = 2.4 \times 10^9$ (Figure 5b). The same behavior is observed in the reference, the 1-minute and 2-minute HF samples, and in all annealed samples. This value is also consistent with previously reported high-power characteristics of superconducting high- Q resonators.^{37,38}

The nonlinear data presented supports the hypothesis that the dominant power-independent loss mechanism in α -Ta samples exposed to HF for 3 minutes and longer is ohmic loss caused by a non-superconducting tantalum hydride. This work reveals previously unreported loss mechanism in α -Ta films, similarly to what was found for Nb resonators.²²

Conclusions

In summary, we have demonstrated that prolonged HF exposure of α -Ta superconducting films introduces a measurable amount of hydrogen into the α -Ta bcc crystal structure, as confirmed by ToF-SIMS, ERDA, and XPS. Additionally, extended HF exposure leads to increased power-independent microwave loss and eventually suppressing the resonance response in high- Q resonators, which is hypothesized to be attributed to the formation of non-superconducting tantalum hydride. Nonlinear resonator analysis further supports this hypothesis, revealing an anomalous two-photon loss mechanism and increased Kerr nonlinearity in samples exposed to HF for 3 minutes or longer. However, we show that annealing at 500°C in UHV effectively removes hydrogen and restores high- Q performance, bringing Q_i values back to those of lightly HF-treated samples. Our results establish a direct link between hydrogen incorporation and microwave loss in α -Ta films, offering a clear strategy to reverse hydrogen-induced degradation in Ta- and Nb-based superconducting

quantum devices. This key insight unlocks the potential for more effective etching and cleaning processes in device fabrication, paving the way for enhanced reliability in next-generation superconducting qubits.

Methods

Multiple sample sets were prepared and characterized in this study to validate the effects of HF treatment on Ta films. The resonator sample underwent HF treatment and annealing were analyzed using microwave characterization and STEM measurements. A separate sample set was used for AFM, XPS, and ToF-SIMS measurements, both after HF treatment and after annealing. Additionally, two more sample sets were analyzed with XPS to confirm that the Ta $4f_{5/2}$ and Ta $4f_{7/2}$ shift was caused by the HF treatment. Finally, a separate sample set was used for ERDA measurements. All HF treatments were performed at different times.

Scanning Transmission Electron Microscopy (STEM)

STEM was performed on samples coated with spin-on carbon (SOC) layer. Lamellae with thickness of <50 nm were cut with focused ion beam (FIB) using Helios 450. For this study, HAADF-STEM were used to investigate metal-air, substrate-air and substrate-metal interfaces.

Time-of-Flight Secondary Ion Mass Spectrometry (ToF-SIMS)

ToF-SIMS measurements were performed using a TOFSIMS NCS instrument from ION-TOF GmbH. Negative ion profiles were measured in a dual beam configuration using a Bi⁺ (15 keV) gun for analysis and a Cs⁺ (500 eV) gun for sputtering, while positive ion profiles were measured in a dual beam configuration using a Bi⁺ (15 keV) gun for analysis and a O₂⁺ (500 eV) gun for sputtering.

Atomic Force Microscopy (AFM)

The AFM measurements were performed using the system ICON PT with equipped with Nanoscope V in a tapping mode configuration. The tip used was OCML-ACI60TS. Both Ta and Si surfaces were scanned across 2x2 μm² areas with a resolution of 2 nm/pixel.

X-ray Photoelectron Spectroscopy (XPS)

The XPS measurements were carried out in Angle Integrated mode using a QUANTES instrument from Physical electronics. The measurements were performed using a monochromatized photon beam of 1486.6 eV. A 100 micron-wide spot was used. Charge neutralization was used during this experiment. Sensitivity factors specific for each instrument were used to convert peak areas to atomic concentrations.

Elastic Recoil Detection Analysis (ERDA)

ERDA experiments utilized a primary ion beam of ³⁵Cl⁴⁺ accelerated to 8 MeV by a 2 MV tandem accelerator. The forward recoiled and scattered ions are detected with a Time of Flight – Energy (ToF-E) telescope. The telescope has a length of 755.4 mm and is installed at a forward scattering angle of 40°. The sample tilt is at 15°. Scattered Cl was used for Ta. Recoil signals were used for the other elements. The reported concentrations refer to atomic fractions: at%.

High-Q resonator measurements

Hanger-type $\lambda/4$ coplanar-waveguide resonators were used to study microwave loss in Ta resonators subject to different post-fabrication treatments as described in the main text. Resonators have resonant frequencies equidistantly spread between 4.2 and 7.8 GHz with coupling Q-factors ranging between 0.2 M and 1.8 M. Central trace width is $w = 24 \mu\text{m}$ and gap between the trace and the ground plane is $s = 12 \mu\text{m}$.

Subdies with 8 resonators are measured in a dilution refrigerator at ~ 10 mK using Keysight P5004 vector network analyzer (VNA). Detailed information on the experimental setup can be found in our previous work^{9,26,40}. Frequency dependent complex scattering parameter S_{21} was measured near the resonance frequency for all resonators as a function of applied microwave power (Figure 5b). Transmission S_{21} scattering parameters are analyzed with an generalized linear resonance model derived for a hanger-type resonator geometry and asymmetric line shapes:^{41,42}

$$S_{21} = A e^{i(\omega t_d + \phi)} \left(1 - \frac{\delta_c}{\delta_c + \delta_i} \frac{e^{i\alpha}}{1 + 2i\tilde{\Delta}} \right), \quad (1)$$

In this expression A is the amplitude of a line shape, t_d is electric delay and ϕ is the phase. α is line shape asymmetry factor. $\delta_i = \kappa_i/\omega_r = 1/Q_i$ is intrinsic loss, $\delta_c = \kappa_c/\omega_r = 1/Q_c$ is coupling loss and $\tilde{\Delta} = \frac{\omega - \omega_r}{\kappa_i + \kappa_c}$ is normalized frequency detuning. Q_i and Q_c are intrinsic and diameter corrected coupling quality factors, respectively, as defined in Ref⁴³.

Intrinsic quality factor shows a characteristic power dependence modelled by the two-level-system loss which is expressed as^{9,44}

$$\delta_i(\bar{n}) = \frac{1}{Q_i(\bar{n})} = \frac{1}{Q_{\text{TLS}}} \frac{\tanh\left(\frac{\hbar\omega_r}{2k_B T}\right)}{\left(1 + \frac{\bar{n}}{n_c}\right)^\alpha} + \delta_0, \quad (2)$$

where $Q_{\text{TLS}} = 1/(F \tan\delta_{\text{TLS}})$, is the two-level-system quality factor. Q_{TLS} is a function of effective energy participation ratio F of interfaces and where TLS defects reside and $\tan\delta_{\text{TLS}}$, which is the intrinsic loss tangent for the material containing the TLS. δ_0 is the contribution from power independent non-TLS loss, n_c is the critical photon number related to the saturation electric field of TLS and α is a phenomenological parameter accounting for geometric effects⁴⁵ and the deviation from the standard TLS model.⁴⁶ Furthermore, \hbar is the Planck constant, ω_r is resonator frequency, k_B is Boltzmann constant and T is the temperature, comparable to the base temperature of the dilution refrigerator with $T_{\text{base}} \sim 10$ mK.

\bar{n} is average photon number in the resonator calculated as⁴⁷ $\bar{n} = \frac{2P_{\text{in}}}{\hbar\omega_r^2} \frac{\delta_c}{(\delta_c + \delta_i)^2}$, where P_{in} is microwave signal power at the input of the resonator. An effective attenuation of approximately 74 dB between the VNA and the resonator inside the dilution refrigerator was separately estimated using ac-Stark shift and χ -shift measurements with a superconducting transmon qubit.⁴⁸

Acknowledgements

The authors gratefully thank Paola Favia, Olivier Richard, Chris Drijbooms, Ilse Hofliijk, Thierry Conard, Céline Noël, Valentina Spampinato, Alexis Franquet and Ryan Leong for metrology support. This work was supported in part by the imec Industrial Affiliation Program on Quantum Computing. We thank L. Swenson and G. Marcaud for insightful comments on this work.

References

1. Acharya, R. *et al.* Quantum error correction below the surface code threshold. *Nature* 1–3 (2024) doi:10.1038/s41586-024-08449-y.
2. Beverland, M. E. *et al.* Assessing requirements to scale to practical quantum advantage. Preprint at <https://doi.org/10.48550/arXiv.2211.07629> (2022).
3. Leon, N. P. de *et al.* Materials challenges and opportunities for quantum computing hardware. *Science* **372**, (2021).
4. Mueller, C., Cole, J. H. & Lisenfeld, J. Towards understanding two-level-systems in amorphous solids: insights from quantum circuits. *Rep. Prog. Phys.* **82**, 124501 (2019).
5. Siddiqi, I. Engineering high-coherence superconducting qubits. *Nat. Rev. Mater.* 1–17 (2021) doi:10.1038/s41578-021-00370-4.
6. Van Damme, J. *et al.* Advanced CMOS manufacturing of superconducting qubits on 300 mm wafers. *Nature* **634**, 74–79 (2024).
7. Place, A. P. M. *et al.* New material platform for superconducting transmon qubits with coherence times exceeding 0.3 milliseconds. *Nat. Commun.* **12**, 1779 (2021).
8. Wang, C. *et al.* Towards practical quantum computers: transmon qubit with a lifetime approaching 0.5 milliseconds. *Npj Quantum Inf.* **8**, 1–6 (2022).
9. Lozano, D. P. *et al.* Low-loss α -tantalum coplanar waveguide resonators on silicon wafers: fabrication, characterization and surface modification. *Mater. Quantum Technol.* **4**, 025801 (2024).

10. Crowley, K. D. et al. Disentangling Losses in Tantalum Superconducting Circuits. *Phys. Rev. X* **13**, 041005 (2023).
11. McLellan, R. A. et al. Chemical Profiles of the Oxides on Tantalum in State of the Art Superconducting Circuits. *Adv. Sci.* **n/a**, 2300921 (2023).
12. Shi, L. et al. Tantalum microwave resonators with ultra-high intrinsic quality factors. *Appl. Phys. Lett.* **121**, 242601 (2022).
13. Marcaud, G. et al. Low-Loss Superconducting Resonators Fabricated from Tantalum Films Grown at Room Temperature. Preprint at <https://doi.org/10.48550/arXiv.2501.09885> (2025).
14. Bal, M. et al. Systematic improvements in transmon qubit coherence enabled by niobium surface encapsulation. *Npj Quantum Inf.* **10**, 1–8 (2024).
15. Pritchard, P. G. & Rondinelli, J. M. Suppressed paramagnetism in amorphous Ta_{5-x}O_{5-x} oxides and its link to superconducting qubit performance. Preprint at <https://doi.org/10.48550/arXiv.2410.13160> (2024).
16. Vargas, P., Miranda, L. & Lagos, M. Diffusion Coefficient of Hydrogen in Niobium and Tantalum*. *Z. Für Phys. Chem.* **164**, 975–983 (1989).
17. Miranda, L., Vargas, P., Cerón, H. & Lagos, M. Hydrogen diffusion in tantalum. *Phys. Lett. A* **131**, 445–448 (1988).
18. Wipf, H. Solubility and diffusion of hydrogen in pure metals and alloys. *Phys. Scr. T* **94**, (2001).
19. Romanenko, A., Barkov, F., Cooley, L. D. & Grassellino, A. Proximity breakdown of hydrides in superconducting niobium cavities. *Supercond. Sci. Technol.* **26**, 035003 (2013).
20. Knobloch, J. The “Q disease” in Superconducting Niobium RF Cavities. *AIP Conf. Proc.* **671**, 133–150 (2003).

21. Sung, Z. *et al.* Direct observation of nanometer size hydride precipitations in superconducting niobium. *Sci. Rep.* **14**, 26916 (2024).
22. Torres-Castanedo, C. G. *et al.* Formation and Microwave Losses of Hydrides in Superconducting Niobium Thin Films Resulting from Fluoride Chemical Processing. *Adv. Funct. Mater.* **34**, 2401365 (2024).
23. Lee, J. *et al.* Discovery of Nb hydride precipitates in superconducting qubits. Preprint at <https://doi.org/10.48550/arXiv.2108.10385> (2021).
24. Murthy, A. A. *et al.* Potential Nanoscale Sources of Decoherence in Niobium based Transmon Qubit Architectures. Preprint at <http://arxiv.org/abs/2203.08710> (2022).
25. Asakawa, T., Nagano, D., Denda, S. & Miyairi, K. Evaluation of Hydrogen in Tantalum Thin Films Using Secondary Ion Mass Spectrometry. *Jpn. J. Appl. Phys.* **47**, 649 (2008).
26. Verjauw, J. *et al.* Investigation of Microwave Loss Induced by Oxide Regrowth in High-Q Niobium Resonators. *Phys. Rev. Appl.* **16**, 014018 (2021).
27. Altoé, M. V. P. *et al.* Localization and Mitigation of Loss in Niobium Superconducting Circuits. *PRX Quantum* **3**, 020312 (2022).
28. Christensen, C., De Reus, R. & Bouwstra, S. Tantalum oxide thin films as protective coatings for sensors. in *Technical Digest. IEEE International MEMS 99 Conference. Twelfth IEEE International Conference on Micro Electro Mechanical Systems (Cat. No.99CH36291)* 267–272 (IEEE, Orlando, FL, USA, 1999). doi:10.1109/MEMSYS.1999.746832.
29. San-Martin, A. & Manchester, F. D. The H-Ta (hydrogen-tantalum) system. *J. Phase Equilibria* **12**, 332–343 (1991).
30. Schober, T. & Wenzl, H. The systems NbH(D), TaH(D), VH(D) : Structures, phase diagrams, morphologies, methods of preparation. in *Hydrogen in Metals II* (eds. Alefeld, G. & Völkl, J.) vol. 29 11–71 (Springer Berlin Heidelberg, Berlin, Heidelberg, 1978).

31. He, X. *et al.* Superconductivity Observed in Tantalum Polyhydride at High Pressure. *Chin. Phys. Lett.* **40**, 057404 (2023).
32. Barkov, F., Romanenko, A., Trenikhina, Y. & Grassellino, A. Precipitation of hydrides in high purity niobium after different treatments. *J. Appl. Phys.* **114**, 164904 (2013).
33. Lizarbe, A. J., Major, G. H., Fernandez, V., Fairley, N. & Linford, M. R. Insight note: X-ray photoelectron spectroscopy (XPS) peak fitting of the Al 2p peak from electrically isolated aluminum foil with an oxide layer. *Surf. Interface Anal.* **55**, 651–657 (2023).
34. Justin Gorham. NIST X-ray Photoelectron Spectroscopy Database - SRD 20. National Institute of Standards and Technology <https://doi.org/10.18434/T4T88K> (2012).
35. Thomas, C. N., Withington, S., Sun, Z., Skyrme, T. & Goldie, D. J. Nonlinear effects in superconducting thin film microwave resonators. *New J. Phys.* **22**, 073028 (2020).
36. Yurke, B. & Buks, E. Performance of Cavity-Parametric Amplifiers, Employing Kerr Nonlinearities, in the Presence of Two-Photon Loss. *J. Light. Technol.* **24**, 5054–5066 (2006).
37. Frasca, S. *et al.* NbN films with high kinetic inductance for high-quality compact superconducting resonators. *Phys. Rev. Appl.* **20**, 044021 (2023).
38. Swenson, L. J. *et al.* Operation of a titanium nitride superconducting microresonator detector in the nonlinear regime. *J. Appl. Phys.* **113**, 104501 (2013).
39. Anferov, A., Suleymanzade, A., Oriani, A., Simon, J. & Schuster, D. I. Millimeter-Wave Four-Wave Mixing via Kinetic Inductance for Quantum Devices. *Phys. Rev. Appl.* **13**, 024056 (2020).
40. Van Damme, J. *et al.* Argon milling induced decoherence mechanisms in superconducting quantum circuits. Preprint at <https://doi.org/10.48550/arXiv.2302.03518> (2023).

41. Rieger, D. *et al.* Fano Interference in Microwave Resonator Measurements. *Phys. Rev. Appl.* **20**, 014059 (2023).
42. Khalil, M. S., Stoutimore, M. J. A., Wellstood, F. C. & Osborn, K. D. An analysis method for asymmetric resonator transmission applied to superconducting devices. *J. Appl. Phys.* **111**, 054510 (2012).
43. Probst, S., Song, F. B., Bushev, P. A., Ustinov, A. V. & Weides, M. Efficient and robust analysis of complex scattering data under noise in microwave resonators. *Rev. Sci. Instrum.* **86**, 024706 (2015).
44. Burnett, J., Bengtsson, A., Niepce, D. & Bylander, J. Noise and loss of superconducting aluminium resonators at single photon energies. *J. Phys. Conf. Ser.* **969**, 012131 (2018).
45. Wang, H. *et al.* Improving the coherence time of superconducting coplanar resonators. *Appl. Phys. Lett.* **95**, 233508 (2009).
46. Phillips, W. A. Tunneling states in amorphous solids. *J. Low Temp. Phys.* **7**, 351–360 (1972).
47. Bruno, A. *et al.* Reducing intrinsic loss in superconducting resonators by surface treatment and deep etching of silicon substrates. *Appl. Phys. Lett.* **106**, 182601 (2015).
48. Koch, J. *et al.* Charge-insensitive qubit design derived from the Cooper pair box. *Phys. Rev. A* **76**, 042319 (2007).
49. McLellan, R. A. *et al.* Chemical Profiles of the Oxides on Tantalum in State of the Art Superconducting Circuits. *Adv. Sci.* **10**, 2300921 (2023).
50. Ranjith, P. M., Rao, M. T., Sapra, S., Suni, I. I. & Srinivasan, R. On the Anodic Dissolution of Tantalum and Niobium in Hydrofluoric Acid. *J. Electrochem. Soc.* **165**, C258–C269 (2018).

51. Chandrasekharan, R., Park, I., Masel, R. I. & Shannon, M. A. Thermal oxidation of tantalum films at various oxidation states from 300 to 700°C. *J. Appl. Phys.* **98**, 114908 (2005).
52. Zhu, M., Zhang, Z. & Miao, W. Intense photoluminescence from amorphous tantalum oxide films. *Appl. Phys. Lett.* **89**, 021915 (2006).
53. Eichler, C. & Wallraff, A. Controlling the dynamic range of a Josephson parametric amplifier. *EPJ Quantum Technol.* **1**, 1–19 (2014).
54. Anferov, A. *et al.* Low-loss Millimeter-wave Resonators with an Improved Coupling Structure. Preprint at <https://doi.org/10.48550/arXiv.2311.01670> (2023).

Supplementary information

Ta and TaO_x etch rates

The etch rate of tantalum oxide was conducted by timed immersion of Ta resonators samples in 10 vol% HF solution. Using atomic force microscopy (AFM), the Ta film height difference was measured between the bottom of the Si resonator gap and the top of the Ta film before and after dipping the samples in HF. Since HF does not attack Si in the range of concentration and treatment durations used in this study, the height difference corresponds to the amount of film removed by the HF. While individual datapoints can be measured with high accuracy, two separate sample sets were measured to gain a better estimate of measurement uncertainty. The first set was immersed for 2, 3, 5, and 10 minutes, while the second set underwent immersion for 8, 9, 10, and 11 minutes. Figure S1 shows that the film thickness remains unchanged up to approximately 9 minutes, with a noticeable reduction visible for 10-minute duration. The 9-minutes step is considered to completely remove the tantalum oxide (~3.7 nm) and marks the beginning of metal tantalum etching. Therefore, we estimate the etching rate of tantalum oxide in a 10 vol% HF solution to be 3.7 nm/9 min = 0.4 nm/min, and the etching rate of the tantalum film to be approximately 15 nm/min. The measured removal of 35 nm of Ta at 10 min is consistent with STEM results shown in Figure 1a.

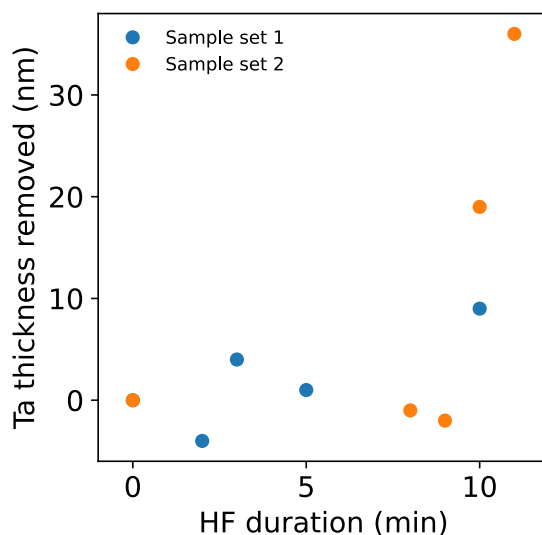


Figure S1: Ta film height thickness removed as a function of HF treatment time.

Surface roughness (AFM)

AFM measurements were performed to analyze how the surface topology of Ta resonators evolves with HF treatment duration and annealing. Surface roughness was determined on both Si and Ta surfaces, with measurements taken after HF treatment and again after HF treatment followed by annealing.

The Ta surface height distribution and mean square roughness (R_q) remains consistent across the reference sample and those treated with HF for 2-3 minutes but shows significant increases in the 5- and 10-minute HF samples [Figure S2(a)]. These surface characteristics persist after annealing at 500°C [Figure S2(b)], indicating the thermal treatment does not alter the surface topology. In contrast, the Si surface exhibits no discernible pattern across any of the samples [Figure S2(c)-(d)]. This confirms our expectations that neither HF treatment nor annealing affects the Si topology, and any observed features can be attributed to the Si recess

generated during the metal etch step in the samples. All the features explained above can also be seen in the AFM maps shown in Figure S3 (a)-(t).

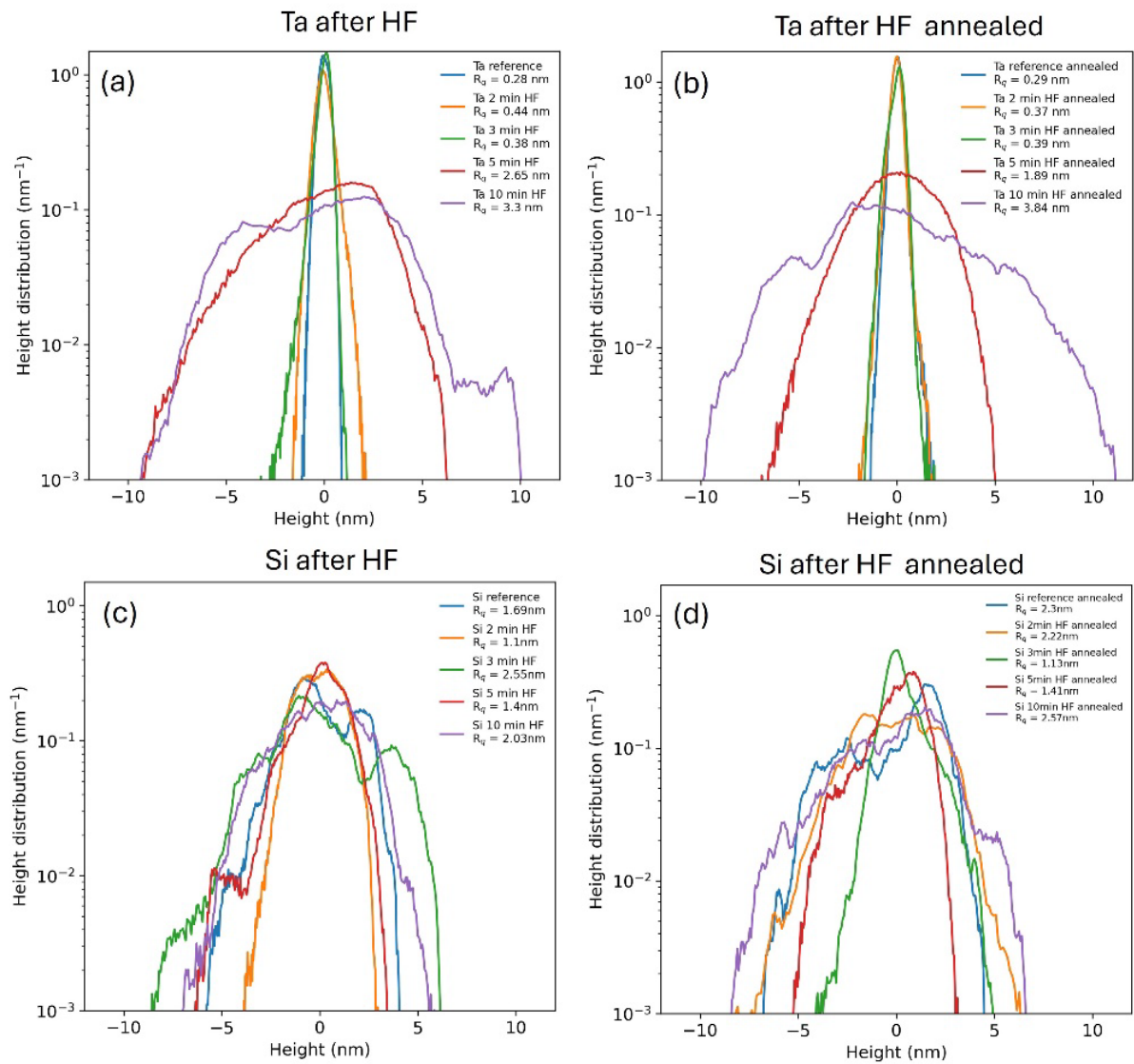


Figure S2: Height distribution on the (a) the Ta surface after the HF treatment, (b) on the Ta surface after the HF treatment and annealing, (c) on the Si surface after the HF treatment and (d) on the Si surface after the HF treatment and the annealing for the reference (blue), 2 min HF (orange), 3 min HF (green), 5 min HF (red) and 10 HF samples (d). The inset list the R_q values for each of the samples.

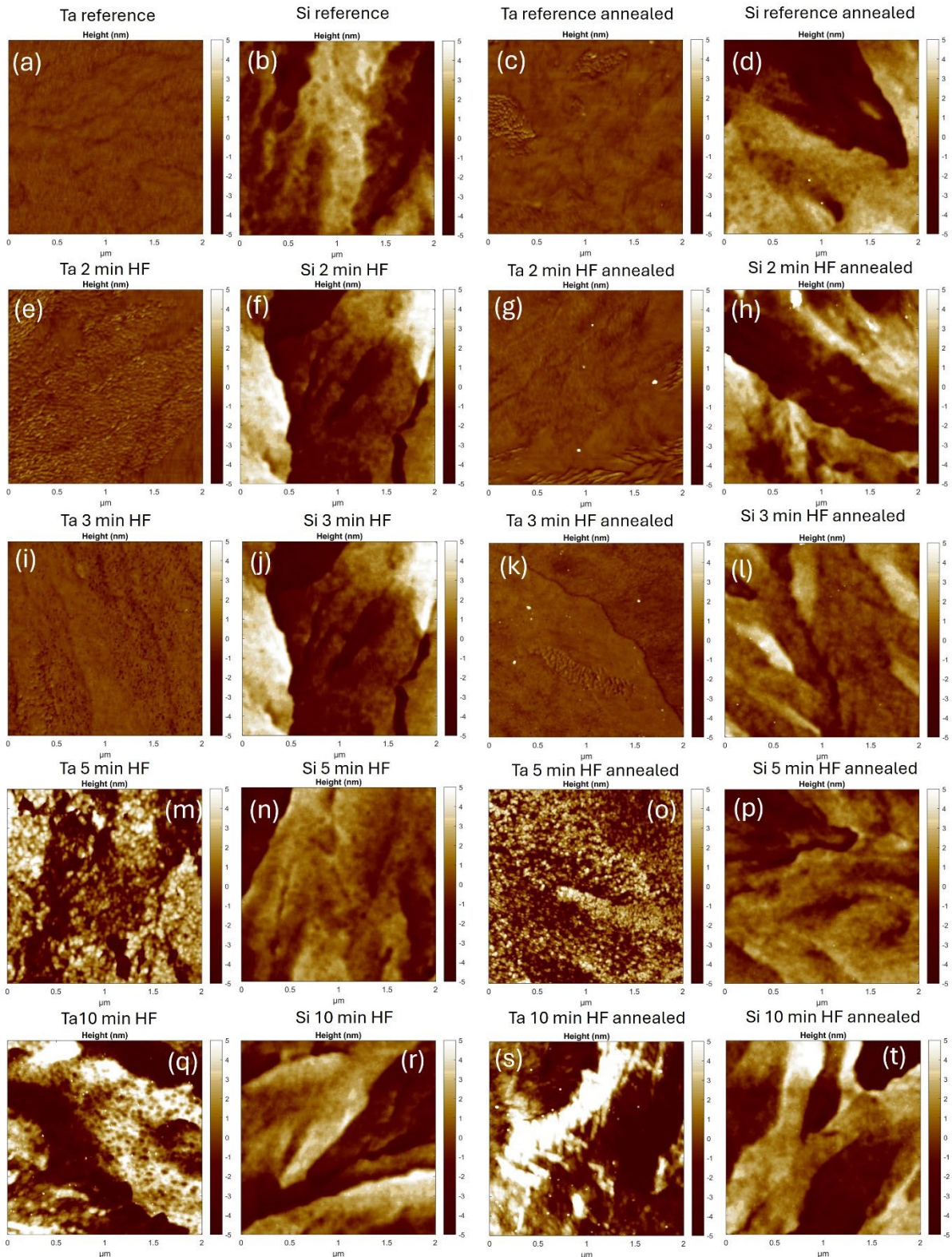


Figure S3: (a)-(t) AFM scans for the Ta and Si surfaces after the HF treatment and after the HF treatment and annealing.

ToF-SIMS characterization

ToF-SIMS technique is used to detect hydrogen and its distribution in the Ta films. Measurements were taken at two stages: after HF treatment and after subsequent annealing. Figure S4 displays the H^+ spectra alongside the $^{30}Si^+$ signal, which was added to clearly mark

the interface between the Ta film and Si substrate. The Ta film thickness of 100 nm was identified at the point where the $^{30}\text{Si}^+$ signal begins to plateau.

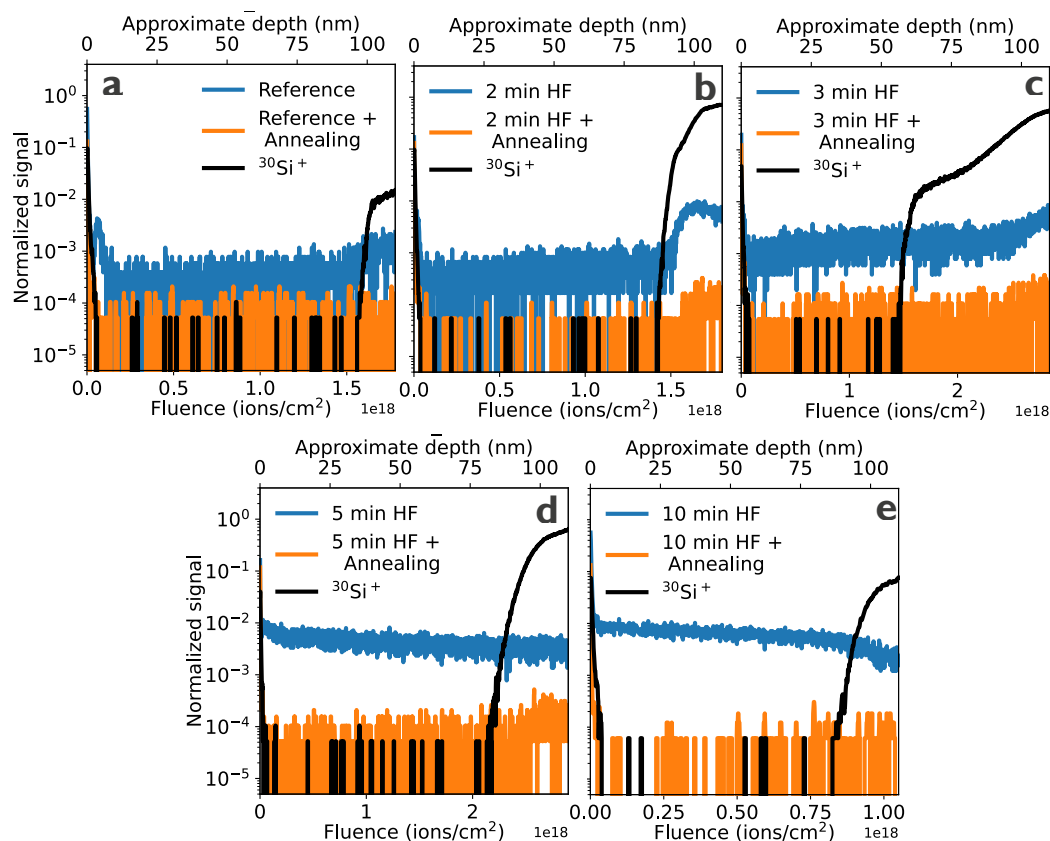


Figure S4: (a)-(e) ToF-SIMS spectra for the H^+ after the HF treatment (blue) and after annealing (orange). The black line indicates the $^{30}\text{Si}^+$ signal. Increase of H^+ signal at the onset of $^{30}\text{Si}^+$ signal for samples with up to 3-minute exposure to HF could be related to changes in H^+ ionization yield or hydrogen gradient established due to its entrance through the triple point.

XPS surface characterization

XPS measurements were performed to analyze the oxide composition on α -Ta film surface. Three distinct sample sets were examined in this study. In sample sets 1 and 3, measurements were performed only after HF treatment at varying durations, while sample set 2 (presented in the main text) underwent two measurement phases: first after HF treatment and second after subsequent annealing. To assess surface variability, three different points were measured on each sample after HF treatment, whereas for sample set 2, only a single point was analyzed post annealing.

The analysis reveals a progressive shift of the Ta4f metallic peaks toward higher binding energies with increasing HF duration, while the Ta4f peaks corresponding to Ta_2O_5 remained stable. Consequently, the binding energy separation between the Ta4f_{7/2} peaks of Ta_2O_5 and metallic Ta decreases, as summarized in Figure S5. This shift is reversible, disappearing after 1-hour UHV annealing at 500°C. Given its reproducibility across three sample sets and reversibility upon annealing, we attribute this behavior to hydrogen absorption and probable tantalum hydride formation rather than charging effects. The presented data supports the findings in the main text (Figure 3) with additional measured samples, improving statistical reliability.

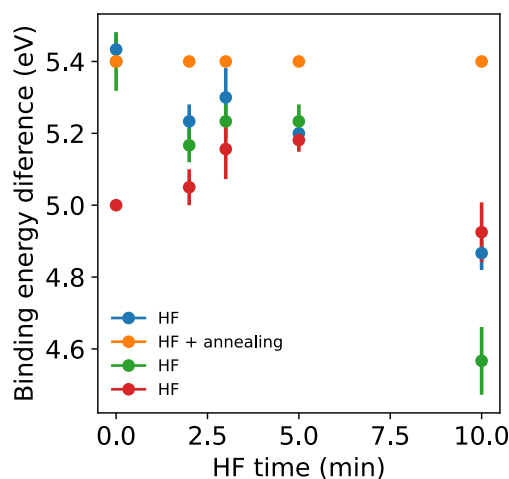


Figure S5: Binding energy difference between the Ta4f_{7/2} oxide and metallic peaks for sample set 1 after HF (blue), sample set 2 after HF (orange), sample set 3 after HF (green) and sample set 2 after HF and annealing (red). Bars represent the standard deviation since each XPS spectrum was measured on 3 different points in the sample sets 1, 2 and 3 after the HF treatment. Sample set two correspond to the data shown in the main text.

To quantitatively determine the amount of tantalum oxide Ta₂O₅, tantalum suboxide (TaO_x) and metallic tantalum components at the surface across sample sets 1, 2, and 3, the Ta4f spectra are fitted with mixed Gaussian-Lorentzian peaks^{9,11} and the relative contributions of individual components are plotted in Figure S6 and summarized in Tables 1-4. While variations in total oxide content exist between sample sets, these differences remain within 15% for any given HF treatment duration. All sample sets exhibited the same trend, which is consistent with our previous results.⁹ Ta₂O₅ is the predominant oxide present in all samples. The total amount of tantalum oxides (Ta₂O₅ + TaO_x) reduces from ~85% to ~70% within the first minute of HF exposure and remains largely unchanged with longer exposure times and subsequent annealing. This suggests that ~1-min HF treatment is sufficient to remove the excess tantalum oxide grown during oxygen-plasma-based resist strip,⁹ while any further removal during prolonged HF exposure is offset by immediate native oxide regrowth.

The atomic fractions of tantalum suboxides (TaO_x) consistently peaked between 2-3 minutes across all sample sets, indicating this pattern as a genuine phenomenon rather than an artifact of single-set measurements. Measured samples show minimum depth values (1.5-2.0 nm) and surface roughness (Rq = 0.27-0.34 nm) that are similar to previous studies in Ta films.⁴⁹ It has been hypothesized that surface roughness and pinholes allow the etching solution to access the buried suboxide layer and modify it. While this is a possible mechanism, the reaction between Ta₂O₅ and HF is a complex four-step dissolution process⁵⁰ involving both sub-oxide and pentoxide intermediates that allow for the rearrangement and removal of oxygen atoms from the tantalum oxide structure. Further studies are needed to clarify how acid treatments can modify the suboxide layers in Ta films.

The amount of suboxides decreases significantly in all annealed samples—for instance, from 7% to 3% in the sample exposed to HF for 2 minutes (Figure S6). This suggests that suboxides undergo further oxidation, converting into Ta₂O₅. This transformation is expected, as Ta₂O₅ is the more thermodynamically stable oxide due to its higher valence state.⁵¹ Metal suboxides like TaO_x typically contain oxygen vacancies caused by deficiency of oxygen atoms in their crystal structure. Upon high-temperature annealing, TaO_x undergoes complete oxidation, reducing oxygen vacancies as it converts into Ta₂O₅.⁵²

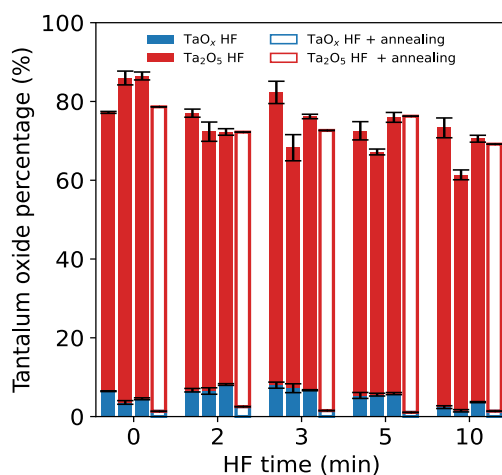


Figure S6: Total tantalum oxide determined from fitting XPS spectra for different samples. Different samples are represented with different bars. The amount of suboxide TaO_x is indicated by the bottom blue part and tantalum oxide Ta_2O_5 amount by the top red part of the bar plot. Annealed samples are indicated by empty bars.

Table 1. Atomic concentrations extracted at different point on the sample surfaces after fitting the XPS spectrum for the Reference, 2 min HF treated, 3 min HF treated, 5 min HF treated, and 10 min HF treated sample set 1.

Reference set 1	C (at%)	O (at%)	Si (at%)	Ta met (at%)	Ta sub.ox (at%)	Ta ₂ O ₅ (at%)
Point 1	28.05	51.50	2.53	2.37	0.83	14.72
Point 2	27.61	51.16	1.66	2.68	0.86	16.02
Point 3	24.45	53.13	2.28	2.75	0.91	16.49
Mean	26.65	51.92	2.12	2.59	0.87	15.73
Standard deviation	1.60	0.86	0.37	0.17	0.03	0.75
HF 2 min set 1						
Point 1	24.81	50.95	1.72	6.58	1.85	14.09
Point 2	23.12	52.85	1.01	6.16	1.81	15.06
Point 3	23.34	52.31	1.56	6.20	1.90	14.68
Mean	23.74	52.03	1.39	6.31	1.85	14.60
Standard deviation	0.75	0.80	0.30	0.19	0.04	0.40
HF 3 min set 1						
Point 1	20.97	55.75	1.41	5.27	1.49	15.12
Point 2	21.00	54.79	1.27	5.44	1.53	15.97
Point 3	21.18	55.13	0.92	5.38	1.50	15.89
Mean	21.05	55.22	1.18	5.36	1.51	15.66
Standard deviation	0.09	0.40	0.21	0.07	0.02	0.38
HF 5 min set 1						
Point 1	29.89	49.32	0.31	4.92	1.21	14.34
Point 2	22.91	53.95	0.73	5.39	1.29	15.74
Mean	26.17	51.58	0.48	5.15	1.25	15.02
Standard deviation	3.49	2.32	0.21	0.24	0.04	0.70
HF 10 min set 1						
Point 1	23.60	52.10	1.85	7.31	0.87	14.27
Point 2	22.85	52.08	1.70	7.87	0.81	14.69
Mean	23.22	52.09	1.77	7.58	0.84	14.48
Standard deviation	0.38	0.01	0.08	0.28	0.03	0.21

Table 2. Atomic concentrations extracted on the sample surface after fitting the XPS spectrum for the Reference + annealing, 2 min HF treated + annealing, 3 min HF treated + annealing, 5 min HF treated + annealing and 10 min HF treated + annealing sample set 1.

Reference + annealing set 1	C (at%)	O (at%)	Si (at%)	Cs (at%)	Ta met (at%)	Ta sub.ox (at%)	Ta2O5 (at%)
Point 1	31.98	46.22	5.97	0.84	3.2	0.2	11.58
HF 2 min + annealing set 1							
Point 1	29.23	47.63	3.96	0.55	5.18	0.47	12.99
HF 3 min + annealing set 1							
Point 1	1.19	46.09	5.08	0.57	4.67	0.26	12.14
HF 5 min + annealing set 1							
Point 1	43.35	38.57	3.58	0.35	3.36	0.15	10.64
HF 10 min + annealing set 1							
Point 1	31.62	45.76	5.47	0.46	5.15	0.23	11.32

Table 3. Atomic concentrations extracted at different point on the sample surfaces after fitting the XPS spectrum for the Reference, 2 min HF treated, 3 min HF treated, 5 min HF treated, and 10 min HF treated sample set 2.

Reference set 2	C (at%)	O (at%)	Si (at%)	Ta met (at%)	Ta sub.ox (at%)	Ta2O5 (at%)
Point 1	24.37	53.78	0.91	3.00	0.76	17.17
Point 2	37.45	43.27	1.74	2.42	0.61	14.51
Point 3	24.42	53.33	0.58	3.03	0.79	17.85
Mean	28.14	49.88	0.97	2.80	0.72	16.44
Standard deviation	6.15	4.85	0.49	0.28	0.08	1.44
HF 2 min set 2						
Point 1	24.37	50.15	1.20	7.31	1.72	15.23
Point 2	21.24	54.25	1.25	5.47	1.29	16.50
Point 3	22.37	51.62	1.53	7.09	1.70	15.69
Mean	22.62	51.98	1.32	6.57	1.56	15.80
Standard deviation	1.29	1.70	0.15	0.82	0.20	0.52
HF 3 min set 2						
Point 1	22.28	51.61	1.20	8.42	1.91	14.58
Point 2	22.46	53.73	1.08	5.99	1.40	15.34
Point 3	21.96	51.46	0.76	8.90	2.04	14.88
Mean	22.23	52.26	0.99	7.66	1.76	14.93
Standard deviation	0.21	1.04	0.19	1.27	0.28	0.31
HF 5 min set 2						
Point 1	23.92	51.76	0.89	7.69	1.33	14.42
Point 2	24.79	50.59	1.27	7.88	1.38	14.08
Point 3	24.26	51.90	0.95	7.29	1.18	14.43
Mean	24.32	51.41	1.02	7.62	1.29	14.31

Standard deviation	0.36	0.59	0.17	0.25	0.08	0.16
HF 10 min set 2						
Point 1	24.73	50.58	1.46	8.99	0.34	13.90
Point 2	23.88	50.48	1.03	9.98	0.48	14.15
Point 3	24.02	52.00	0.61	8.51	0.26	14.60
Mean	24.30	50.53	1.23	9.47	0.40	14.02
Standard deviation	0.43	0.05	0.21	0.50	0.07	0.13

Table 4. Atomic concentrations extracted at different point on the sample surfaces after fitting the XPS spectrum for the Reference, 2 min HF treated, 3 min HF treated, 5 min HF treated, and 10 min HF treated sample set 3.

Reference set 3	C (at%)	O (at%)	Si (at%)	Ta met (at%)	Ta sub.ox (at%)	Ta ₂ O ₅ (at%)
Point 1	24.37	53.78	0.91	3.00	0.76	17.17
Point 2	37.45	43.27	1.74	2.42	0.61	14.51
Point 3	24.42	53.33	0.58	3.03	0.79	17.85
Mean	28.14	49.88	0.97	2.80	0.72	16.44
Standard deviation	6.15	4.85	0.49	0.28	0.08	1.44
HF 2 min set 3						
Point 1	24.37	50.15	1.20	7.31	1.72	15.23
Point 2	21.24	54.25	1.25	5.47	1.29	16.50
Point 3	22.37	51.62	1.53	7.09	1.70	15.69
Mean	22.62	51.98	1.32	6.57	1.56	15.80
Standard deviation	1.29	1.70	0.15	0.82	0.20	0.52
HF 3 min set 3						
Point 1	22.28	51.61	1.20	8.42	1.91	14.58
Point 2	22.46	53.73	1.08	5.99	1.40	15.34
Point 3	21.96	51.46	0.76	8.90	2.04	14.88
Mean	22.23	52.26	0.99	7.66	1.76	14.93
Standard deviation	0.21	1.04	0.19	1.27	0.28	0.31
HF 5 min set 3						
Point 1	23.92	51.76	0.89	7.69	1.33	14.42
Point 2	24.79	50.59	1.27	7.88	1.38	14.08
Point 3	24.26	51.90	0.95	7.29	1.18	14.43
Mean	24.32	51.41	1.02	7.62	1.29	14.31
Standard deviation	0.36	0.59	0.17	0.25	0.08	0.16
HF 10 min set 3						
Point 1	24.73	50.58	1.46	8.99	0.34	13.90
Point 2	23.88	50.48	1.03	9.98	0.48	14.15
Point 3	24.02	52.00	0.61	8.51	0.26	14.60
Mean	24.30	50.53	1.23	9.47	0.40	14.02
Standard deviation	0.43	0.05	0.21	0.50	0.07	0.13

Superconducting T_c measurements

Superconducting transition temperature is measured for samples exposed to HF for different times using a four-probe measurement in an adiabatic demagnetization refrigeration (ADR)

cryostat. We can see that reference sample show the lowest $T_c = 4.20$ K, while samples exposed to HF between 2- and 5-minute exhibit somewhat higher values of $T_c = 4.25$ K (Figure S7). This increase could be a result of reduced amount of total Ta oxide on the surface. Surprisingly, the sample that was exposed to HF for 10 minutes show no superconducting transition down to 0.2 K. This is likely due to the considerable amount of TaH_x (close to δ phase) in the metal which can render the entire film non-superconducting.

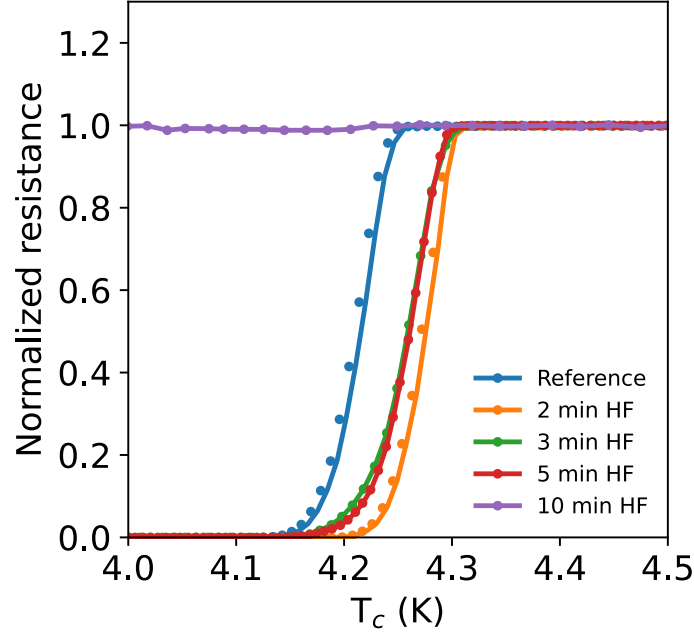


Figure S7: Normalized resistance measurements as a function of temperature for Ta samples show superconducting transition at approximately $T_c = 4.25$ K for samples exposed to HF of up to 5min, and no transition for 10-minute exposed sample down to 0.2 K (not shown).

Nonlinear high-Q resonator modeling

In this section we describe the nonlinear model and a fitting strategy for measured S21 scattering parameter as a function of frequency for Ta resonators exposed to diluted HF for 3min (Figure 5). The nonlinear fitting model encompasses both nonlinear kinetic inductance (L) contribution as well as nonlinear ohmic loss (R) modelled with two-photon absorption contributions³⁶

$$L = \Delta L \left(1 + \frac{I^2}{I_c^2} \right), \quad R = \Delta R \left(1 + \frac{I^2}{I_c^2} \right), \quad (3)$$

where I and I_c are current and critical current, respectively. Both contributions arise when microwave current density through a superconducting transmission or a strip line becomes overcritical at its peak near the edges, in which case reduced Cooper pair density and increased quasiparticle density at the edges lead to current dependent kinetic inductance and resistance per unit length.^{35,36}

The nonlinear Kerr effect is modelled with the following Hamiltonian,

$$\mathcal{H} = \hbar\omega_r a^\dagger a + \frac{\hbar}{2} K_{nl} a^\dagger a^\dagger a a, \quad (4)$$

and the two-photon loss is accounted for with the following equation of motion,

$$\dot{a} = -i\omega_r a - iK_{\text{nl}} a^\dagger a a - \frac{\kappa_i + \kappa_c}{2} a - \frac{\gamma_{\text{nl}}}{2} a^\dagger a a - \sqrt{\frac{\kappa_c}{2}} a_{\text{in}}. \quad (5)$$

In the above two expressions, \hbar is the Planck constant divided by 2π , ω_r is the resonator's fundamental frequency, K_{nl} is the nonlinear Kerr parameter, γ_{nl} is the nonlinear two-photon loss parameter, κ_i is internal loss rate, κ_c is coupling rate to the feedline, a^\dagger and a are creation and annihilation operators obeying bosonic commutation relation $[a, a^\dagger] = 1$ and a_{in} is incoming drive photon flux.

Assuming coherent drive ($a(t) = a e^{-i\omega t}$) and multiplying both sides of Eq. (5) with its complex conjugate we arrive at the nonlinear equation for inter resonator photon number,

$$\frac{\kappa_c}{2} |a_{\text{in}}|^2 = n^3 \left(K_{\text{nl}}^2 + \frac{\gamma_{\text{nl}}^2}{4} \right) + 2n^2 \left[\frac{(\kappa_i + \kappa_c)\gamma_{\text{nl}}}{4} - \Delta K_{\text{nl}} \right] + n \left[\frac{(\kappa_i + \kappa_c)^2}{4} + \Delta^2 \right], \quad (6)$$

where $n = a^\dagger a$ is intra-resonator photon number and $\Delta = \omega - \omega_r$ is frequency difference between the drive and the resonator's fundamental resonant mode.

Eq. (6) can be further simplified by normalizing the equation to^{53,54}

$$\frac{1}{2} = \tilde{n}^3 \left(\xi^2 + \frac{\eta^2}{4} \right) + 2\tilde{n}^2 \left[\frac{\eta}{4} - \xi \tilde{\Delta} \right] + \tilde{n} \left[\frac{1}{4} + \tilde{\Delta}^2 \right], \quad (7)$$

where

$$\tilde{n} = \frac{n}{|\tilde{a}_{\text{in}}|^2}, \quad \xi = \frac{|\tilde{a}_{\text{in}}|^2 K_{\text{nl}}}{\kappa_i + \kappa_c}, \quad \eta = \frac{|\tilde{a}_{\text{in}}|^2 \gamma_{\text{nl}}}{\kappa_i + \kappa_c}, \quad \tilde{\Delta} = \frac{\Delta}{\kappa_i + \kappa_c}, \quad |\tilde{a}_{\text{in}}|^2 = \frac{\kappa_c}{(\kappa_i + \kappa_c)^2} |a_{\text{in}}|^2.$$

When calculating the scattering parameter of a nonlinear resonator, the third order nonlinear Eq. (7) is solved first to obtain \tilde{n} as a function of frequency $\tilde{\Delta}$, which is then used to expand the Lorentzian line shape¹ as follows:

$$S_{21} = A e^{i(\omega t_d + \phi)} \left(1 - \frac{\delta_c}{\delta_c + \delta_i} \frac{e^{i\alpha}}{1 + \eta \tilde{n} + 2i(\tilde{\Delta} - \xi \tilde{n})} \right), \quad (8)$$

In the above expression $\xi \tilde{n} = \frac{K_{\text{nl}} n}{\kappa_i + \kappa_c}$ is the normalized nonlinear frequency shift and $\eta \tilde{n} = \frac{\gamma_{\text{nl}} n}{\kappa_i + \kappa_c}$ is the normalized nonlinear two-photon loss rate, with $K_{\text{nl}} \cdot n$ and $\gamma_{\text{nl}} \cdot n$ being nonlinear Kerr shift and two-photon loss rate, respectively.

The nonlinear frequency shift can lead to an asymmetric tilted Duffing response of $S_{21}(\omega)$ or a multi-solution response beyond the critical bifurcating point for $\xi < \xi_c$. Notably, $S_{21}(\omega)$ measurement points form a circle in an IQ plane across all parameter regimes, even for drive powers beyond the bifurcation point. Conversely, the nonlinear two-photon loss term results in a non-circular resonance curve in the IQ plane. This resonance curve takes on an approximately elliptical shape with the $S_{21}(\omega_r)$ and asymptotic $S_{21}(\omega \rightarrow \pm\infty)$ points located

¹ This line shape expression is adapted from Daniel Flanigan resonator package (<https://github.com/danielflanigan>) which is rewritten for convenient fitting with the lmfitt python package.

at the co-vertices, the endpoints of the minor axis.^{35,36} In the limit where $\xi \rightarrow 0$ and $\eta \rightarrow 0$, Eq. (8) converges to the linear generalized asymmetric Lorentzian line shape [Eq. (1)].⁴³

The high-power scattering parameter data shown in Figure 5c,d is modelled by the following nonlinear fitting procedure implemented using the *lmfit* python package. Starting with initial set of fitting parameters the photon number is computed for each frequency point using Eq. (7). These photon numbers and the remaining fitting parameters are used to compute the scattering parameter S21 as a function of frequency using Eq. (8). The nonlinear fitting is performed using the least square method (*leastsq*) from *scipy.optimize* package used by *lmfit*.

The nonlinear Kerr parameter (K_{nl}) and the nonlinear two-photon loss parameter (γ_{nl}) are obtained by repeating the described fitting routine for S21 spectra collected at higher microwave drive powers (empty markers in Figure S8a,b) and plotting nonlinear Kerr shift ($K_{nl} \cdot n$) and two-photon loss rate ($\gamma_{nl} \cdot n$) against the maximum photon number in a resonator. The nonlinear Kerr parameter and the two-photon loss parameter are finally extracted from the slope of the linear fit (Figure S8c,d), which are for Ta resonators exposed to diluted HF for 3 min summarized in Figure S8e. Surprisingly, K_{nl} and γ_{nl} have comparable values ranging from 0.5 to 3 kHz. This is possibly due to a common quasiparticle heating source.

Total internal quality factor combining linear intrinsic and the nonlinear loss $Q_i^{-1} = \frac{\kappa_i}{\omega_r} + \frac{\gamma_{nl}n}{\omega_r}$ extracted for each S21 spectrum at a given power agree well with a combination of a TLS intrinsic loss model (2) and a two-photon loss from a single parameter for each resonator presented in Figure S8e as shown with a dashed line in Figure S8a,b.

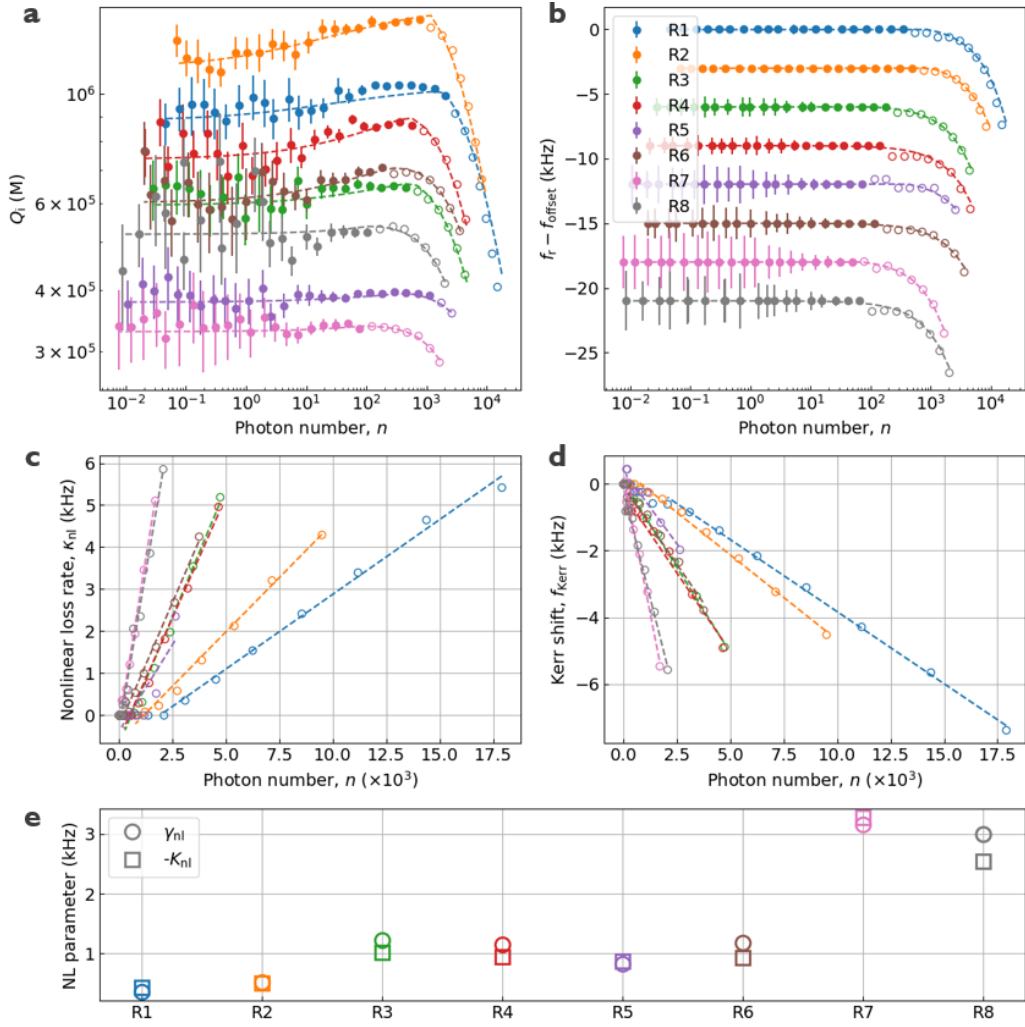


Figure S8: Nonlinear analysis of Q -internal and resonator frequency shift for all 8 resonators on a Ta resonator sample exposed to 3min HF. **a** Internal Q -factor as a function of photon number in a resonator. Dashed lines correspond to total linear and nonlinear loss. **b** Resonator's frequency shift relative to their value at the lowest photon number as a function of the photon number in a resonator. For better visibility, data for each resonator is offset by 3 kHz. Dashed lines indicate nonlinear Kerr shift. **c** Nonlinear loss rate as a function of photon number and **d** Kerr shift as a function of the photon number. **e** nonlinear loss (γ_{nl}) and negative nonlinear Kerr ($-\kappa_{nl}$) parameters extracted from slopes in subpanels **c** and **d** for each resonator on a chip.

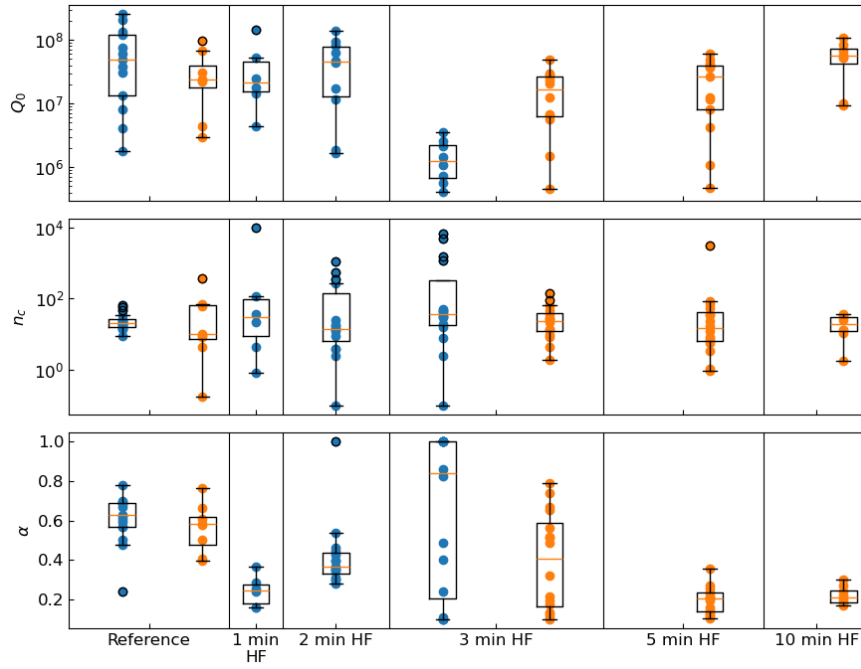


Figure S9: Summary of TLS model fitting parameters for different resonators with different HF treatment. High-power S_{21} measurements that exhibit nonlinear behaviour were excluded from TLS model fitting Eq. (2) presented here. Parameters plotted here are: Q_0 power-independent loss, n_c critical photon number, and α is the phenomenological parameter accounting for geometric effects.